

# Inverse Dynamics Trajectory Optimization for Contact-Implicit Model Predictive Control

Journal Title  
XX(X):1–16  
©The Author(s) 2023  
Reprints and permission:  
sagepub.co.uk/journalsPermissions.nav  
DOI: 10.1177/ToBeAssigned  
www.sagepub.com/

SAGE

Vince Kurtz<sup>1,3</sup>, Alejandro Castro<sup>2</sup>, Aykut Özgün Önal<sup>2</sup>, and Hai Lin<sup>3</sup>

## Abstract

Robots must make and break contact with the environment to perform useful tasks, but planning and control through contact remains a formidable challenge. In this work, we achieve real-time contact-implicit model predictive control with a surprisingly simple method: inverse dynamics trajectory optimization. While trajectory optimization with inverse dynamics is not new, we introduce a series of incremental innovations that collectively enable fast model predictive control on a variety of challenging manipulation and locomotion tasks. We implement these innovations in an open-source solver and present simulation examples to support the effectiveness of the proposed approach. Additionally, we demonstrate contact-implicit model predictive control on hardware at over 100 Hz for a 20-degree-of-freedom bi-manual manipulation task. Video and code are available at <https://idto.github.io>.

## Keywords

Model predictive control, contact-implicit trajectory optimization, contact-planning, legged locomotion, manipulation.

## 1 Introduction

Contact is critical for legged locomotion and dexterous manipulation, but most optimization-based controllers assume a fixed contact sequence (Wensing et al. 2022). Contact-Implicit Trajectory Optimization (CITO) aims to relax this assumption by solving jointly for the contact sequence and a continuous motion. A sufficiently performant CITO solver would enable Contact-Implicit Model Predictive Control (CI-MPC), allowing robots to determine contact modes on the fly and perform more complex tasks.

Despite growing interest in CITO, fast and reliable CI-MPC remains elusive. Most existing methods take either a direct approach (Posa and Tedrake 2013; Manchester et al. 2019; Winkler et al. 2018; Patel et al. 2019; Moura et al. 2022; Wang et al. 2023; Aydinoglu et al. 2023; Cleac’h et al. 2023), in which decision variables represent state and control at each time step, or a shooting approach (Tassa et al. 2012; Neunert et al. 2017; Carus et al. 2018; Chatzinikolaïdis and Li 2021; Kim et al. 2022; Howell et al. 2022c; Kong et al. 2022), where control inputs are the only decision variables. Both work well for smooth dynamical systems, but struggle to handle contact. The large number of additional constraints used to model contact, rank deficiency, and ill conditioning have a large impact on numerics. Poor numerics in turn degrade robustness, convergence, and performance. Other issues include the difficulty of initializing and/or warm-starting variables, locally optimal solutions that do not obey physics, and high sensitivity to problem parameters. Much active research focuses on solving these problems.

Here, we adopt a less popular approach, Inverse Dynamics Trajectory Optimization (IDTO) (Erez and Todorov 2012; Todorov 2019a), and show that it enables fast and effective CI-MPC. Instead of constraints, IDTO uses compliance and regularized friction to formulate an optimization problem

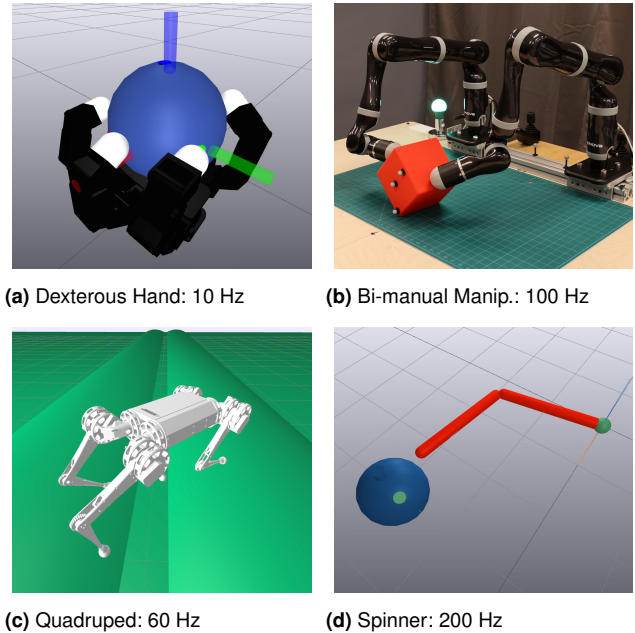


**Figure 1.** IDTO enables real-time CI-MPC on a variety of challenging manipulation and locomotion tasks. Contact sequences, locations, and timings are all determined automatically by the solver over a 1-2 second horizon.

<sup>1</sup>Department of Civil and Mechanical Engineering, California Institute of Technology, USA

<sup>2</sup>Toyota Research Institute, USA

<sup>3</sup>Department of Electrical Engineering, University of Notre Dame, USA

## Corresponding author:

Vince Kurtz, California Institute of Technology, 1200 E California Blvd, Pasadena, CA 91125, USA

Email: vkurtz@caltech.edu

where generalized positions are the only decision variables. We cast this optimization as a least squares problem, for which we develop a custom trust-region solver. This solver leverages a series of small innovations—a smooth and compliant contact model, scaling, sparse Hessian factorization, and an equality-constrained dogleg method—to achieve state-of-the-art performance. Despite using a relaxed contact model, our IDTO solver enables high-performance real-time CI-MPC on systems with rigid contact. We demonstrate this performance on a variety of simulation examples (where the simulator uses a rigid contact model) as well as on hardware, as shown in Fig. 1.

## 2 Related Work

This section reviews related literature, categorizing methods based on offline CITO versus online CI-MPC.

### 2.1 Contact-Implicit Trajectory Optimization

CITO aims to optimize the robot’s trajectory, contact forces, and actuation. Different formulations exist, depending primarily on the choice of decision variables.

Direct methods introduce decision variables for both state and control, and enforce the dynamics with constraints (Posa and Tedrake 2013; Manchester et al. 2019; Winkler et al. 2018; Patel et al. 2019; Moura et al. 2022; Wang et al. 2023). This results in a large but sparse nonlinear program. Direct methods support arbitrary constraints and infeasible initializations. However, the large number of nonlinear constraints used to model dynamics and contact lead to a large optimization problem, which is difficult to solve efficiently. Moreover, these formulations can fall into local minima that might not obey physics (Posa et al. 2016).

Shooting methods like Differential Dynamic Programming (DDP) (Mayne 1966) and iterative LQR (iLQR) (Li and Todorov 2004) introduce decision variables only for the control, and are increasingly popular for CITO (Tassa et al. 2012; Neunert et al. 2017; Carius et al. 2018; Chatzinikolaïdis and Li 2021; Kim et al. 2022; Howell et al. 2022c). These methods enforce dynamics with forward rollouts, so each iteration is dynamically feasible. On the other hand, designing an informative initial guess can be challenging, and it is difficult to include constraints. Additionally, each rollout simulates contact dynamics to high precision, which usually requires solving an optimization sub-problem for each time step (Castro et al. 2022). Combining the flexibility of direct methods with the defect-free integration of shooting is an area of active research (Önol et al. 2019, 2020; Suh et al. 2022; Gifftthaler et al. 2018).

### 2.2 Contact-Implicit Model Predictive Control

The earliest simulated CI-MPC (Tassa et al. 2012) ran in real time for low-dimensional problems, but could not maintain real-time performance for larger systems. The first hardware implementation (Neunert et al. 2018) emerged several years later, though this method required extensive parameter tuning.

Recent years have seen numerous exciting advancements in CI-MPC. MuJoCo MPC (Howell et al. 2022a) enables real-time CI-MPC for a number of larger systems

(quadrupeds, humanoids, etc.) using various algorithms. Cleac’h et al. (2023) achieved quadruped CI-MPC on hardware with a bi-level scheme, performing more expensive computations offline about a reference trajectory and solving smaller problems online with a sparse interior-point solver.

Kim et al. (2023) take a shooting approach, using a mixture of compliant and rigid contact models. A rigid complementarity-based model is used for forward rollouts, while gradients are computed based on a smooth relaxation that allows force at a distance. They demonstrate the performance of this approach in impressive hardware experiments with a quadruped robot.

Kong et al. (2022) introduce a hybrid-systems iLQR method, with sophisticated mechanisms for handling unexpected contact mode transitions, and demonstrate real-time CI-MPC on a quadruped. Another hybrid MPC approach based on the Alternating Direction Method of Multipliers (ADMM) (Aydinoglu et al. 2023) breaks the dependence of the contact-scheduling problem between time steps, allowing parallelization. The ADMM method enables a contact-rich ball-rolling task on hardware.

### 2.3 Inverse Dynamics Trajectory Optimization

While most existing work treats inputs as the decision variables (shooting methods) or states and inputs as the decision variables (most direct methods), IDTO uses only generalized positions (Erez and Todorov 2012).

This offers several advantages. Inverse dynamics are faster to compute than the forward dynamics needed in shooting methods (Ferrolho et al. 2021). Unlike typical direct methods, IDTO does not require complex dynamics constraints, and uses compliant contact to eliminate the need for contact constraints. Early CITO work used IDTO and simplified physics to synthesize contact-rich behaviors for animated characters (Mordatch et al. 2012a,b). Erez and Todorov (2012) proposed a physically consistent version, and Emo Todorov described a more mature implementation in Optico, an unreleased software package, in several talks (Todorov 2019a,b). Our work is heavily inspired by Optico, though we believe our solver differs in a number of important respects. We use trust region rather than linesearch, for example, and handle underactuation differently.

A drawback of IDTO is the need for compliant contact, as contact forces must be a function of state. Much of the community holds complementarity-based rigid contact as the gold standard for physical realism in planning and simulation (Howell et al. 2022b; Aydinoglu et al. 2023; Kim et al. 2023). Nonetheless, all contact models are approximations, and strict complementarity can introduce non-physical artifacts that are even more severe than those in compliant models (Castro et al. 2023, Section IV.A). In this paper, we introduce a compliant contact model with physics-based relaxations, and show that CI-MPC over this relaxed model performs well on systems with rigid contact. In all of our simulation experiments, we plan using the relaxed model but simulate using Drake’s state-of-the-art model of rigid contact (Tedrake and the Drake Development Team 2019).

### 3 Contribution

In this paper, we show that IDTO enables real-time CI-MPC for complex systems like those shown in Fig. 1. We detail design choices for the *formulation* as a least-squares problem and develop a custom *solver* for that problem.

Our implementation is available at <https://idto.github.io>. In this paper, we describe implementation details, characterize numerics and convergence, and evaluate performance. We validate our solver in simulation for a variety of dexterous manipulation and legged locomotion tasks, as well as on hardware for bi-manual manipulation. While our solver uses a relaxed contact model, our simulation experiments use the state-of-the-art physics in Drake (Tedrake and the Drake Development Team 2019).

Our approach is not perfect, nor is it the ultimate CI-MPC solution. We strove to make simple design choices whenever possible, with the hope that this will illuminate key challenges and pave the way to better solutions in the future. To this end, we provide an extensive discussion of the limitations of our approach in Section 8.

### 4 Nonlinear Least-Squares Formulation

We closely follow the notation of our previous work on contact modeling for simulation (Castro et al. 2020, 2022). We use  $\mathbf{x} = [\mathbf{q} \ \mathbf{v}]$  to describe the state of a multibody system, consisting of generalized positions  $\mathbf{q} \in \mathbb{R}^{n_q}$  and generalized velocities  $\mathbf{v} \in \mathbb{R}^{n_v}$ . Time derivatives of the positions relate to velocities by the kinematic map  $\mathbf{N}(\mathbf{q}) \in \mathbb{R}^{n_q \times n_v}$ ,

$$\dot{\mathbf{q}} = \mathbf{N}(\mathbf{q})\mathbf{v}. \quad (1)$$

$\mathbf{N}(\mathbf{q})$  is the identity matrix in most cases, though not for quaternion Degrees of Freedom (DoFs).

We consider CITO problems of the form

$$\min_{\mathbf{x}, \mathbf{u}} \int_{t=0}^T \ell(\mathbf{x}(t), \mathbf{u}(t), t) dt + \ell_f(\mathbf{x}(T)), \quad (2a)$$

$$\text{s.t. } \mathbf{M}(\mathbf{q})\dot{\mathbf{v}} + \mathbf{k}(\mathbf{q}, \mathbf{v}) = \mathbf{B}\mathbf{u} + \mathbf{J}^T \mathbf{f}, \quad (2b)$$

$$\mathbf{x}(0) = \mathbf{x}_0. \quad (2c)$$

The cost (2a) encodes the task and penalizes actuation, where  $\ell$  and  $\ell_f$  are running and terminal costs respectively. The problem is constrained to satisfy the equations of motion (2b), where  $\mathbf{M}$  is the mass matrix,  $\mathbf{k}$  collects gyroscopic terms, gravitational forces and joint damping, and  $\mathbf{B}$  maps actuation inputs  $\mathbf{u} \in \mathbb{R}^{n_u}$  to actuated DoFs. The dynamics (2b) include both the robot and objects in the environment. For a set of  $n_c$  contact constraints, contact forces  $\mathbf{f} \in \mathbb{R}^{3n_c}$  are applied through the contact Jacobian  $\mathbf{J} \in \mathbb{R}^{3n_c \times n_v}$ . Finally, (2c) provides the initial condition at time  $t = 0$ .

#### 4.1 Contact Kinematics

Given a configuration  $\mathbf{q}$ , our contact engine reports a set of  $n_c$  contact pairs. We characterize the  $i$ -th pair by its location, signed distance  $\phi_i(\mathbf{q}) \in \mathbb{R}$  and contact normal  $\hat{\mathbf{n}}_i$ , see (Castro et al. 2022) for details. The relative velocity at the contact point is denoted  $\mathbf{v}_{c,i}$ , and relates to generalized velocities via the  $i$ -th row of the contact Jacobian. We split the contact velocity into its normal component  $v_{n,i} = \hat{\mathbf{n}}_i \cdot \mathbf{v}_{c,i}$  and tangential component  $\mathbf{v}_{t,i} = \mathbf{v}_{c,i} - v_{n,i}\hat{\mathbf{n}}_i$ , so that

$\mathbf{v}_{c,i} = [v_{n,i} \ \mathbf{v}_{t,i}]$ . For brevity, we omit the contact subscript  $i$  from now on.

#### 4.2 Contact Modeling

Many CITO formulations augment (2) with additional decision variables and constraints to model contact forces that satisfy Coulomb friction and the principle of maximum dissipation. Building on our experience in contact modeling for simulation (Castro et al. 2020, 2022), we adopt a simpler approach based on compliant contact with regularized friction. With this approach, contact forces are a function of state. Unlike the accurate and often stiff models used for simulation, however, here we focus on algebraic forms that are continuously differentiable and thus more suitable for trajectory optimization. As we will show in Section 6, this relaxed contact model enables performant CI-MPC in simulations with a more realistic model of rigid contact as well as on hardware.

As with the contact velocity, we split the contact force at each contact point into its normal  $f_n$  and tangential  $\mathbf{f}_t$  components such that  $\mathbf{f}_c = [f_n \ \mathbf{f}_t]$ . The key aspects of our contact model are illustrated in Fig. 2, and detailed below.

We model the normal force as

$$f_n = c(\phi)d(v_n), \quad (3)$$

where

$$c(\phi) = \sigma k \log(1 + \exp(-\phi/\sigma)) \quad (4)$$

provides a smooth model of compliance that approximates a linear spring of stiffness  $k$  in the limit to zero smoothing parameter  $\sigma$  (Fig. 2a). While  $\sigma$  can be thought of as the scale parameter of a logistic distribution over signed distances  $\phi$  (Pang et al. 2023), here we use it to trade off smoothness and force at a distance.  $\sigma$  takes length units, and should be set according to the scale of the system in question.

We model dissipation as

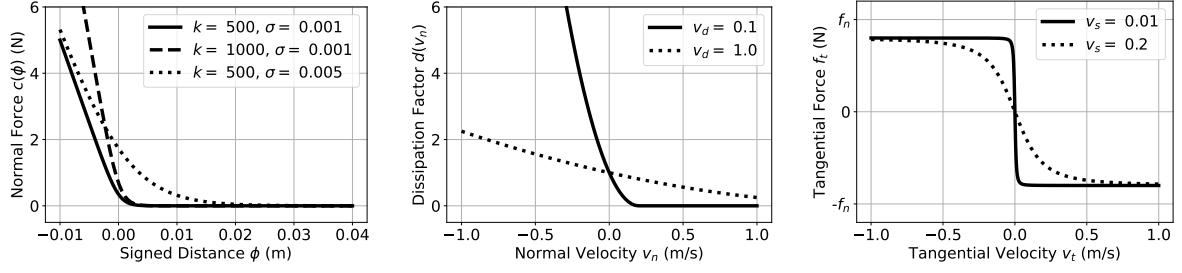
$$d(v_n) = \begin{cases} 1 - \frac{v_n}{v_d} & \text{if } \frac{v_n}{v_d} < 0, \\ (\frac{v_n}{v_d} - 2)^2/4 & \text{if } 0 \leq \frac{v_n}{v_d} < 2, \\ 0 & \text{if } 2 \leq \frac{v_n}{v_d}, \end{cases} \quad (5)$$

a smoothed Hunt and Crossley model (Hunt and Crossley 1975) with dissipation velocity  $v_d = 1/d_{HC}$  the reciprocal of the Hunt and Crossley dissipation parameter  $d_{HC}$  (Fig. 2b). The intuition behind this model is as follows: if two bodies are moving toward each other,  $d(v_n)$  increases the effective stiffness of the contact. Conversely, if the bodies are moving away from each other ( $v_n > 0$ ), the effective stiffness is reduced. This helps avoid large interpenetrations while also limiting the “bounciness” of the contact.

We model the tangential component  $\mathbf{f}_t$  with a regularized model of Coulomb friction

$$\mathbf{f}_t = -\mu \frac{\mathbf{v}_t}{\sqrt{v_s^2 + \|\mathbf{v}_t\|^2}} f_n, \quad (6)$$

where  $\mu$  is the friction coefficient and  $v_s$  is the *stiction tolerance* (Fig. 2c). This model satisfies both the model of Coulomb friction ( $\|\mathbf{f}_t\| \leq \mu f_n$ ) and the principle of maximum dissipation (friction opposes velocity) at the expense of drift during stiction at speeds lower than  $v_s$ .



(a) Stiffness component  $c(\phi)$  (4). (b) Dissipation component  $d(v_n)$  (5). (c) Regularized friction (6) with  $\mu = 0.8$ .

**Figure 2.** Visualization of our compliant contact model (4)-(6) for various parameter values. This model is differentiable everywhere, but introduces force-at-a-distance (a) and drift-during-stiction (c) artifacts.

**4.2.1 Choosing Contact Parameters** Unlike contact modeling for simulation, where the principal objective is to model physical dynamics as faithfully as possible, contact modeling for CI-MPC has two competing goals: (1) model the system accurately, and (2) maintain a friendly optimization landscape. Modeling choices that improve physical accuracy, like high stiffnesses and tight friction regularization, also make the optimization problem more difficult, inducing narrow valleys and steep walls in the cost landscape.

As we will show in Section 6, CI-MPC feedback is able to make up for significant modeling errors. As a result, we recommend choosing contact parameters *as soft/highly regularized as possible, while maintaining good closed-loop performance with a rigid simulator*. Table 1 lists each of the parameters in our contact model, along with its physical meaning and our tuning recommendations.

While contact parameter tuning is an ad-hoc and problem-specific process, the rapid feedback enabled by a fast solver like IDTO does make parameter tuning easier. This could be further improved with a graphical interface that allows for tuning in real-time, as in Howell et al. (2022a). Additionally, each of the contact parameters has a clear physical interpretation, which can guide the tuning process. This is not the case for all common contact models, as illustrated in (Castro et al. 2023, Section IV).

### 4.3 Inverse Dynamics Trajectory Optimization

In this section, we approximate (2) as a nonlinear least squares problem. The key idea is to use generalized positions  $\mathbf{q}$  as the only decision variables and enforce dynamic feasibility with inverse dynamics.

We will focus on quadratic cost terms of the form

$$\begin{aligned} \ell(\mathbf{x}, \mathbf{u}, t) &= \frac{1}{2} \|\mathbf{x}(t) - \bar{\mathbf{x}}(t)\|_{\mathbf{Q}}^2 + \frac{1}{2} \|\mathbf{u}(t)\|_{\mathbf{R}}^2, \\ \ell_f(\mathbf{x}) &= \frac{1}{2} \|\mathbf{x}(T) - \bar{\mathbf{x}}(T)\|_{\mathbf{Q}_f}^2, \end{aligned} \quad (7)$$

where  $\mathbf{Q}$ ,  $\mathbf{R}$ , and  $\mathbf{Q}_f$  are diagonal scaling matrices and  $\bar{\mathbf{x}}(\cdot)$  is a nominal trajectory.  $\bar{\mathbf{x}}(\cdot)$  outlines a desired behavior and is not necessarily dynamically feasible.

We discretize the time horizon into  $N$  steps of size  $\delta t$  and approximate (2a) using a first-order quadrature rule

$$L(\mathbf{x}, \mathbf{u}) = \sum_{k=0}^N \ell_k(\mathbf{x}_k, \mathbf{u}_k), \quad (8)$$

where for convenience we define the total cost  $L(\mathbf{x}, \mathbf{u})$ ,  $\ell_k = \delta t \ell(\mathbf{x}_k, \mathbf{u}_k)$ , and  $\ell_N = \ell_f(\mathbf{x}_N)$ .

We then proceed to write (8) in terms of generalized positions  $\mathbf{q}$ .<sup>\*</sup> Velocities  $\mathbf{v}$  are a function of  $\mathbf{q}$  as follows,

$$\mathbf{v}_k(\mathbf{q}) = \mathbf{N}^+(\mathbf{q}_k) \frac{\mathbf{q}_k - \mathbf{q}_{k-1}}{\delta t} \quad \forall k = 1 \dots N, \quad (9)$$

where  $\mathbf{N}^+(\mathbf{q}_k)$  is the left pseudoinverse of the kinematic mapping matrix (1).  $\mathbf{v}_0 = \mathbf{v}(0)$  is given by (2c).

Similarly, we approximate accelerations  $\mathbf{a}$  as

$$\mathbf{a}_k(\mathbf{q}) = \frac{\mathbf{v}_{k+1}(\mathbf{q}) - \mathbf{v}_k(\mathbf{q})}{\delta t} \quad \forall k = 0 \dots N-1. \quad (10)$$

Note that we use  $k+1$  and  $k$  for accelerations, while we use  $k$  and  $k-1$  for velocities. This leads to  $\mathbf{a}_k$  that depend symmetrically on  $\mathbf{q}_{k-1}$ ,  $\mathbf{q}_k$ , and  $\mathbf{q}_{k+1}$ .

We write contact forces  $\mathbf{f}$  as a function of  $\mathbf{q}$  using the compliant contact model outlined in Section 4.2,

$$\mathbf{f}_k(\mathbf{q}) = \mathbf{f}(\mathbf{q}_{k+1}, \mathbf{v}_{k+1}(\mathbf{q})) \quad \forall k = 0 \dots N-1. \quad (11)$$

Finally, we use inverse dynamics to define the generalized forces  $\boldsymbol{\tau}_k$  needed to advance the state from time step  $k$  to time step  $k+1$ ,

$$\begin{aligned} \boldsymbol{\tau}_k(\mathbf{q}) &= \mathbf{M}(\mathbf{q}_{k+1})\mathbf{a}_k + \mathbf{k}(\mathbf{q}_{k+1}, \mathbf{v}_{k+1}) \\ &\quad - \mathbf{J}^T(\mathbf{q}_{k+1})\mathbf{f}_k(\mathbf{q}_{k+1}, \mathbf{v}_{k+1}). \end{aligned} \quad (12)$$

When compared to a time-stepping scheme for simulation (Castro et al. 2022), all terms are evaluated *implicitly*. We make this choice based on the intuition that implicit time-stepping schemes are stable even for stiff systems of equations. The accuracy and usefulness of this intuition in the IDTO setting is an important area for future study.

For fully actuated systems, generalized forces equal control torques,  $\boldsymbol{\tau}_k = \mathbf{u}_k$ . In the more typical underactuated case, we have  $\boldsymbol{\tau}_k = \mathbf{B}\mathbf{u}_k$ , and some entries of  $\boldsymbol{\tau}_k$  must be zero. Substituting both  $\boldsymbol{\tau}_k$  and  $\mathbf{x}_k = [\mathbf{q}_k \ \mathbf{v}_k]$  as functions of  $\mathbf{q}$  in (8), we can approximate (2) as,

$$\min_{\mathbf{q}} L(\mathbf{q}), \quad (13a)$$

$$\text{s.t. } \mathbf{h}(\mathbf{q}) = 0, \quad (13b)$$

where  $\mathbf{h}(\mathbf{q})$  collects unactuated rows of  $\boldsymbol{\tau}_k(\mathbf{q})$ .

<sup>\*</sup>We denote the vector of all configurations with  $\mathbf{q} = [\mathbf{q}_0, \mathbf{q}_1, \dots, \mathbf{q}_N]$  and similarly all velocities  $\mathbf{v} = [\mathbf{v}_0, \mathbf{v}_1, \dots, \mathbf{v}_N]$ .



**Table 1.** Summary of contact parameters and tuning recommendations.

Symbol	Units	Physical meaning	Tuning recommendation
$k$	N/m	Spring stiffness for contact normal force.	Set as low as possible while maintaining good closed-loop MPC performance with a rigid simulator.
$\sigma$	m	Amount of force-at-a-distance/smoothing factor.	Scale with the size of the system in question, set as large as possible while maintaining closed-loop performance.
$v_d$	m/s	Dissipation velocity: lower values correspond to stiffer and less bouncy contact.	0.1 m/s worked well for all of the systems we tried.
$\mu$	-	Friction coefficient.	Set according to the physical system in question.
$v_s$	m/s	Stiction velocity: the speed at which bodies in stiction slide.	Set as high as possible while maintaining good closed-loop MPC performance with a rigid simulator.

**Remark 1.** This is a nonlinear least squares problem with equality constraints. To see this, define the residual

$$\mathbf{r}(\mathbf{q}) = \begin{bmatrix} \tilde{\mathbf{Q}}^{1/2}(\mathbf{x}(\mathbf{q}) - \bar{\mathbf{x}}) \\ \tilde{\mathbf{R}}^{1/2}\boldsymbol{\tau}(\mathbf{q}) \end{bmatrix} \quad (14)$$

where  $\tilde{\mathbf{Q}}$  and  $\tilde{\mathbf{R}}$  denote the diagonal matrices that result from stacking  $\mathbf{Q}$  and  $\mathbf{R}$ . We can then write the cost in standard least squares form:  $L(\mathbf{q}) = 1/2\|\mathbf{r}(\mathbf{q})\|^2$ .

## 5 Gauss-Newton Trust-Region Solver

In this section, we develop a solver tailored to (13).

### 5.1 The Unconstrained Problem

We start by considering the unconstrained problem, for which we choose a trust-region method. At each iteration  $i$ , this method finds an update  $\mathbf{q}^{i+1} = \mathbf{q}^i + \mathbf{p}$  by solving a quadratic approximation of (13) around  $\mathbf{q}^i$ ,

$$\min_{\mathbf{p}} L^i + \mathbf{g}^T \mathbf{p} + \frac{1}{2} \mathbf{p}^T \mathbf{H} \mathbf{p} \quad (15a)$$

$$\text{s.t. } \|\mathbf{D}^{-1} \mathbf{p}\| \leq \Delta, \quad (15b)$$

where  $L^i = L(\mathbf{q}^i)$  and  $\mathbf{g} = \nabla L(\mathbf{q}^i)$  are the cost and its gradient. Matrix  $\mathbf{H}$  is a Gauss-Newton approximation of the Hessian, see Section 5.3 for details. At each iteration, the trust-region constraint (15b) limits the size of the step  $\mathbf{p}$ . We use a diagonal matrix  $\mathbf{D}$  to scale the problem and improve numerical conditioning. Stiff contact dynamics result in a cost landscape with narrow valleys and steep walls. This makes scaling critical for good performance, as illustrated in Fig. 3. We tried various strategies (Moré 2006), and found that  $\text{diag}(\mathbf{D}) = \text{diag}(\mathbf{H})^{-1/4}$  gave the best results.

Since solving (15) exactly would be computationally expensive, we use the *dogleg method* (Nocedal and Wright 2006, §4.1) to find an approximate solution. This requires a single update and factorization of  $\mathbf{H}$  per iteration. After each iteration, we update the trust-region radius  $\Delta$  with a standard strategy (Nocedal and Wright 2006, Algorithm 4.1).

**Remark 2.** We chose trust region over linesearch for several reasons. One is speed: each evaluation of the cost  $L(\mathbf{q})$  is expensive, and trust region requires us to compute  $L(\mathbf{q})$  only once per iteration. Trust region is also appealing because  $\mathbf{H}$  is poorly conditioned. In some extreme instances, this

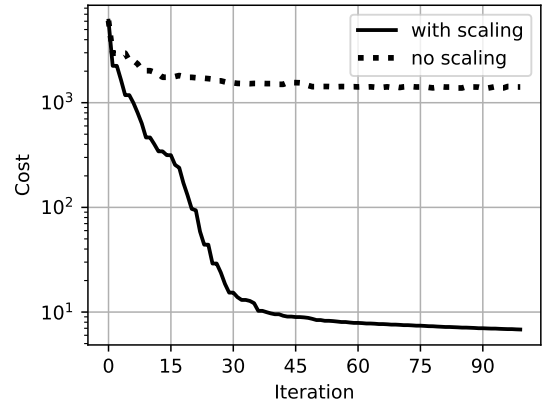


**Figure 3.** Convergence plot for the Allegro hand example with and without scaling.

can lead to Gauss-Newton search directions ( $\mathbf{p} = -\mathbf{H}^{-1}\mathbf{g}$ ) that are not actually descent directions due to floating point error. Trust-region methods turn toward gradient descent as the trust radius is reduced, which helps avoid this issue.

### 5.2 Handling Equality Constraints

For systems of practical interest with unactuated DoFs, enforcing (13b) is critical for dynamic feasibility. We consider two methods to handle this constraint.

**5.2.1 Quadratic Penalty** This method adds a penalty of the form  $\frac{w}{2}\|\mathbf{h}(\mathbf{q})\|^2$  to the cost  $L(\mathbf{q})$ , where  $w$  is a large scalar weight. In practice we implement this by placing  $w$  at elements of  $\mathbf{R}$  that correspond to unactuated DoFs.

**5.2.2 Lagrange Multipliers** The penalty method is simple to implement, and worked well in many cases. However, it cannot entirely drive unactuated torques to zero without high penalties that worsen numerics.

As an alternative, we developed a constrained dogleg method based on Lagrange multipliers. We start with a constrained Newton step

$$\begin{bmatrix} \mathbf{H} & \mathbf{A}^T \\ \mathbf{A} & \mathbf{0} \end{bmatrix} \begin{bmatrix} \mathbf{p} \\ \boldsymbol{\lambda} \end{bmatrix} = \begin{bmatrix} -\mathbf{g} \\ -\mathbf{h} \end{bmatrix}, \quad (16)$$

where  $\mathbf{A}$  is the Jacobian of  $\mathbf{h}$  and  $\boldsymbol{\lambda}$  is a vector of Lagrange multipliers. Since our Hessian approximation is invertible, we can eliminate  $\mathbf{p}$  from (16) and solve for

$$\boldsymbol{\lambda} = (\mathbf{A} \mathbf{H}^{-1} \mathbf{A}^T)^{-1} (\mathbf{h} - \mathbf{A} \mathbf{H}^{-1} \mathbf{g}). \quad (17)$$

We then solve (16) for the Newton step

$$\mathbf{p} = -\mathbf{H}^{-1}(\mathbf{A}^T \boldsymbol{\lambda} + \mathbf{g}). \quad (18)$$

We can view this step as the unconstrained minimizer of a quadratic model of the merit function

$$L(\mathbf{q}) + \mathbf{h}(\mathbf{q})^T \boldsymbol{\lambda}. \quad (19)$$

This observation motivates a trust-region variant, where we minimize a quadratic model of (19) subject to bounds on the step size. More formally, the new trust-region subproblem is given by

$$\min_{\mathbf{p}} L(\mathbf{g} + \mathbf{A}^T \boldsymbol{\lambda})^T \mathbf{p} + \frac{1}{2} \mathbf{p}^T \mathbf{H} \mathbf{p} \quad (20a)$$

$$\text{s.t. } \|\mathbf{D}^{-1} \mathbf{p}\| \leq \Delta, \quad (20b)$$

which we can solve with the dogleg method. This approach is similar to Fletcher's smooth exact penalty method (Nocedal and Wright 2006), albeit with a slightly different approximation of the Lagrange multipliers  $\boldsymbol{\lambda}$ .

Computing  $\boldsymbol{\lambda}$  efficiently does take some care. We use our sparse factorization of  $\mathbf{H}$  to compute  $\mathbf{H}^{-1} \mathbf{A}^T$  one column at a time. We then form a dense  $\mathbf{A} \mathbf{H}^{-1} \mathbf{A}^T$  matrix and solve for  $\boldsymbol{\lambda}$  with a dense Cholesky factorization. It should be possible to exploit the sparse structure of  $\mathbf{A} \mathbf{H}^{-1} \mathbf{A}^T$  to perform this inversion more efficiently, but we have not done so for this work.

### 5.3 Sparse Gauss-Newton Hessian Approximation

Note that  $\ell_k$  does not depend on the full configuration sequence  $\mathbf{q}$  but only on the stencil  $\mathbf{q}_{k-1}, \mathbf{q}_k, \mathbf{q}_{k+1}$ ,

$$\ell_k(\mathbf{x}_k(\mathbf{q}), \boldsymbol{\tau}_k(\mathbf{q})) = \ell_k(\mathbf{q}_{k-1}, \mathbf{q}_k, \mathbf{q}_{k+1}). \quad (21)$$

Therefore the  $k$ -th segment of the gradient,  $\mathbf{g}_k$ , can be computed as

$$\begin{aligned} \frac{\partial L(\mathbf{q})}{\partial \mathbf{q}_k} &= \mathbf{g}_k(\mathbf{q}_{k-2}, \mathbf{q}_{k-1}, \mathbf{q}_k, \mathbf{q}_{k+1}, \mathbf{q}_{k+2}) \\ &= \frac{\partial \ell_{k-1}}{\partial \mathbf{q}_k} + \frac{\partial \ell_k}{\partial \mathbf{q}_k} + \frac{\partial \ell_{k+1}}{\partial \mathbf{q}_k}. \end{aligned} \quad (22)$$

Using the chain rule through the quadratic costs in (7), we can write the terms in (22) as

$$\frac{\partial \ell_k}{\partial \mathbf{q}_s} = (\mathbf{x}_k - \bar{\mathbf{x}}_k)^T \mathbf{Q} \frac{\partial \mathbf{x}_k}{\partial \mathbf{q}_s} + \boldsymbol{\tau}_k^T \mathbf{R} \frac{\partial \boldsymbol{\tau}_k}{\partial \mathbf{q}_s}, \quad (23)$$

for  $s = k - 1 \dots k + 1$ .

Given that the gradient in (22) involves a stencil with five time steps, the Hessian inherits a pentadiagonal sparsity structure

$$\mathbf{H}_{k,s} = \frac{\partial \mathbf{g}_k}{\partial \mathbf{q}_s} \quad \forall s = k - 2 \dots k + 2. \quad (24)$$

We exploit this structure by factorizing  $\mathbf{H}$  with a block-sparse variation of the Thomas algorithm (Benkert and Fischer 2007).

While it is possible to compute the first and second derivatives of inverse dynamics analytically (Carpentier and

Mansard 2018; Singh et al. 2022), obtaining analytical derivatives through contact is significantly more challenging, given the complex kinematics involved (Cui and Dai 2010). This motivates a Gauss-Newton approximation. Applying the chain rule through (23) and neglecting second-order derivatives leads to an approximation in terms of generalized velocity and inverse dynamics gradients,

$$\mathbf{H}(\mathbf{q}) \approx \mathbf{H} \left( \frac{\partial \mathbf{v}}{\partial \mathbf{q}}, \frac{\partial \boldsymbol{\tau}}{\partial \mathbf{q}} \right), \quad (25)$$

with the full expression given in Appendix 9.

We approximate the velocity gradients as

$$\begin{aligned} \frac{\partial \mathbf{v}_k}{\partial \mathbf{q}_k} &= \frac{1}{\delta t} \mathbf{N}^+(\mathbf{q}_k^i), \\ \frac{\partial \mathbf{v}_{k+1}}{\partial \mathbf{q}_k} &= -\frac{1}{\delta t} \mathbf{N}^+(\mathbf{q}_{k+1}^i), \end{aligned}$$

where we have frozen  $\mathbf{N}^+$  at the previous iteration  $i$ .

For the inverse dynamics gradients, we use finite differences. This is computationally intensive since it requires many inverse dynamics evaluations and geometry queries. These derivatives are the most time-consuming portion of IDTO, as shown by the profiling in Section 6.

**Remark 3.** Computing gradients through contact requires a contact engine at least as accurate as the finite difference step size. We found that geometry computations based on iterative methods (Gilbert et al. 1988) do not provide the required accuracy and lead to inaccurate gradients. Furthermore, geometries with sharp corners (e.g., boxes) induce discontinuous jumps in the contact normal  $\hat{\mathbf{n}}$ , rendering finite difference derivatives useless. We therefore restricted ourselves to analytical geometry computations accurate to machine precision, and replaced collision geometries with inscribed spheres or half-spaces.

While analytical gradients could greatly improve solver speed and accuracy, computing them efficiently remains a significant challenge. To the best of our knowledge, existing analytical methods like Carpentier et al. (2019) do not account for the variations in contact location. In particular, the contact jacobian  $\mathbf{J}$  depends on the location of contact points. Contact location then depends on collision geometries and varies in a way that is not captured by analytical methods designed for trajectory optimization with fixed contact sequences. For this reason, our solver relies on a simple finite-difference approach.

## 6 Results

Here we characterize the performance of our IDTO solver on the four systems shown in Fig. 1. In all simulation examples, the simulator uses Drake's state-of-the-art model of rigid contact, while the planner uses the compliant model described in Section 4.2.

### 6.1 Test Cases

**6.1.1 Spinner** The spinner is a 3-DoF system shown in Fig. 1d. The two finger links are 1 m long and mass 1 kg, with a diameter of 0.05 m. The spinner itself is a 1 kg sphere with a 0.25 m radius. The target trajectory  $\bar{\mathbf{x}}$  rotates the spinner 2 radians while the finger remains stationary at the initial position, with the finger tip 0.08 m from the spinner.

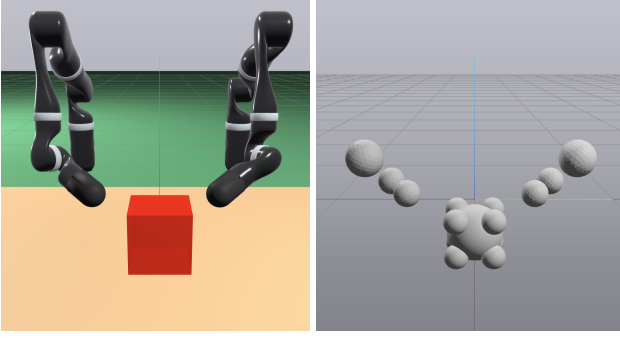


**Figure 4.** Visual (left) and collision (right) geometries for the bi-manual manipulation task. We eliminate sharp corners by modeling the box with inscribed spheres. Additionally, we only include arm collision geometries near the end-effectors. IDTO is able to overcome the resulting modeling error in both simulations (using box collisions) and hardware experiments.

**6.1.2 Mini Cheetah Quadruped** Mini Cheetah (Fig. 1c) is a 9 kg quadruped with 18 DoFs (12 actuated joints and a floating base) (Katz et al. 2019). The robot is tasked with moving in a desired direction and matching a desired orientation. We model hills as 1 m diameter cylinders embedded in the ground.

Unlike most existing work on CI-MPC for quadrupeds (Winkler et al. 2018; Cleac’h et al. 2023; Kong et al. 2022; Howell et al. 2022a), we do not specify a preferred gait sequence. Rather, the robot is merely asked to move in the desired direction, with a small terminal cost encouraging the legs to end the trajectory in a standing configuration.

**6.1.3 Allegro Dexterous Hand** Our highest-DoF example is a dexterous manipulation task with the simulated Allegro hand shown in Fig. 1a. The ball is a 50 g sphere with a 6 cm radius. The overall system has 22 DoFs—16 actuated in the hand and 6 unactuated for the ball.

The hand is to rotate the ball so that the colorful marks on the ball line up with a target set of axes, shown as a transparent triplet in Fig. 1a and the accompanying video. The nominal trajectory  $\bar{x}$  consists of the ball rotating while the hand remains stationary in a nominal “holding” configuration.

**6.1.4 Bi-Manual Manipulator** Finally, we consider the bi-manual manipulation task shown in Fig. 1b. This consists of two Kinova Jaco arms and a 550 g uniform density cube with 15 cm sides. The system has 20 DoFs: 14 actuated joints in the arms plus the box’s floating base. As discussed in Remark 3, finite differences impose smoothness and accuracy requirements on the geometry queries, so we model the box with 9 inscribed spheres, as shown in Fig. 4.

The target trajectory  $\bar{x}$  moves the box to a desired pose while keeping the arms stationary in their initial configuration. We consider three tasks, each defined by a different target pose: moving the box along the table, lifting the box up, and balancing the box on its edge.

## 6.2 Parameters

Table 2 reports contact and planning parameters for each example system. Note that these contact parameters are used by the optimizer for planning, but not by the simulator.

**Table 2.** Contact model and planning parameters.

	Spinner	Quadruped	Allegro	Bi-Manual
Stiffness (N/m)	200	2000	100	1000
Smoothing (cm)	1.0	1.0	0.1	0.5
Friction Coeff.	0.5	1.0	1.0	0.2
Stiction (m/s)	0.05	0.5	0.1	0.05
Time Step (s)	0.05	0.05	0.05	0.05
Horizon (s)	2.0	1.0	2.0	1.0

Contact stiffness scales with the expected magnitude of contact forces, as well as the amount of penetration we are willing to accept. The smoothing factor is determined primarily by the size of the system, with smaller systems requiring a smaller smoothing length scale. Numerical considerations dominate the choice of stiction velocity: small values model stiction more accurately, but large values result in a smoother problem for the optimizer.

For the cost weights ( $Q, R, Q_f$ ), we use diagonal matrices with values reported in Table 3. The final row specifies a quadratic penalty on torques applied to unactuated DoFs. Note that for the quadruped, we apply a different weight for the floating base position and orientation in the running cost.

## 6.3 Open-Loop Trajectory Optimization

For each of the examples described above, we performed open-loop optimization with both the penalty method and the Lagrange multipliers (LM) method (see Section 5.2). Convergence plots are shown in Fig. 5. This figure shows the cost and constraint violations (sum of squared generalized forces on unactuated DoFs) at each iteration. Since underactuation constraints are the only dynamics constraints in IDTO, constraint violations provide a measure of dynamic feasibility.

The LM method sometimes performed much better than the penalty method (spinner and Allegro hand), and occasionally found higher-quality local minima. This is shown in the spinner example, where the penalty was not sufficient to drive the finger to touch the spinner, leading to a high cost and large constraint violations.

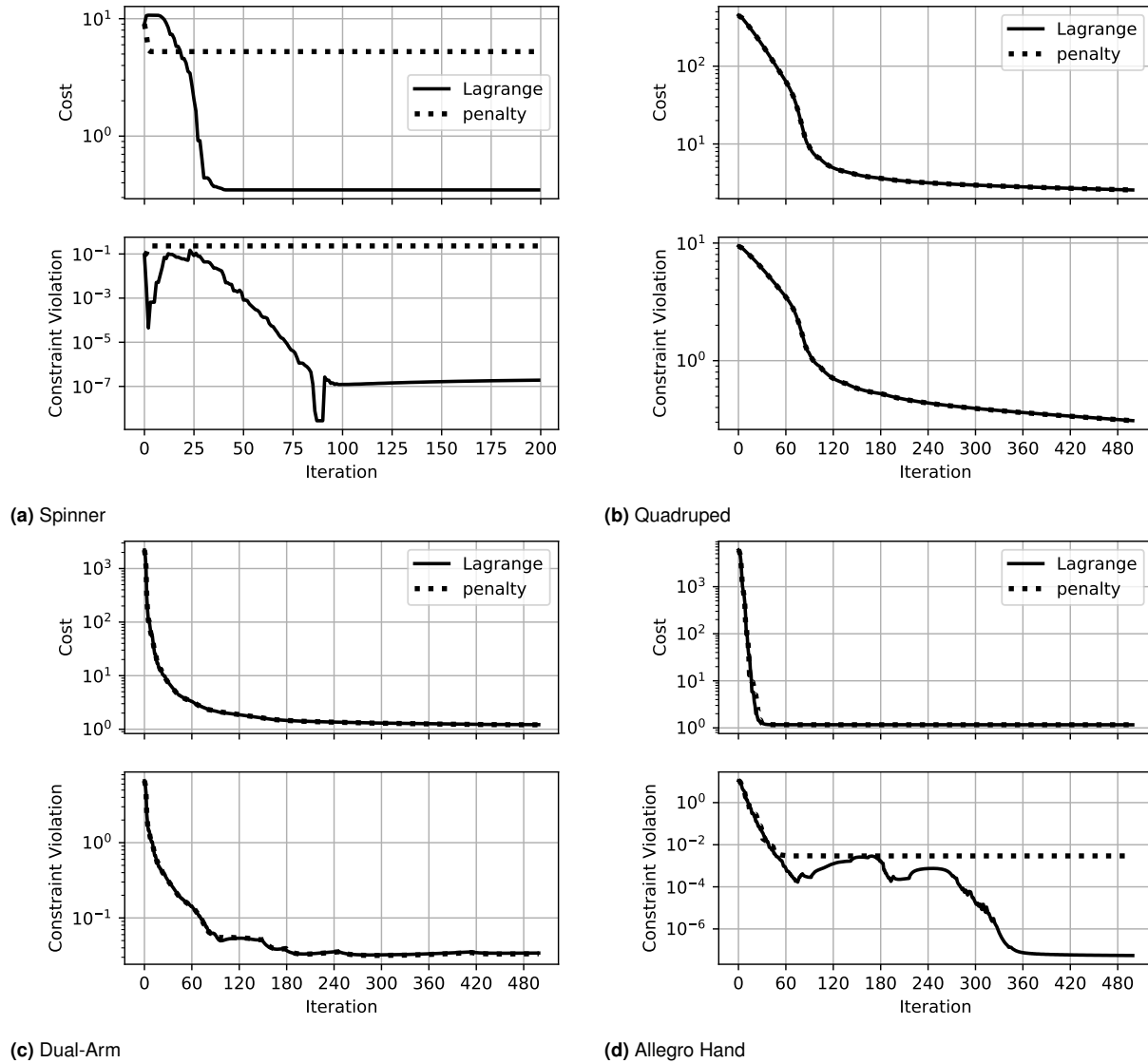
For the quadruped and bi-manual manipulation cases, the two methods produced nearly identical results. In these cases, the penalty method is preferable due to the cost of solving  $\lambda$  from (17). This additional cost is illustrated in Fig. 6, which plots the average wall-clock time per iteration for different planning horizons. With the penalty method, complexity is linear in the planning horizon and cubic in the number of DoFs, similar to iLQR/DDP. Scalability is worse with the LM method: our current implementation solves (17) using dense algebra, rendering complexity cubic in the planning horizon.

We emphasize that the convergence shown in Fig. 5 is not particularly good: for many of the examples, constraint violations are still large and the cost is still slowly decreasing even after 500 iterations. However, we found these solutions to be informative in offline CITO computations, particularly with the quick user interaction cycles enabled by the speed of these computations. For MPC, we found that high control rates compensate for poor convergence accuracy.

Figure 7 shows a breakdown of the computational cost, using a 2 s (40 step) horizon for all of the examples.

**Table 3.** Cost weights for each example system.

	Spinner			Quadruped			Allegro			Bi-Manual		
	$Q$	$R$	$Q_f$	$Q$	$R$	$Q_f$	$Q$	$R$	$Q_f$	$Q$	$R$	$Q_f$
actuated positions	1	-	10	0	-	1	0.01	-	1	0	-	0.1
unactuated positions	1	-	10	10 (pos.), 1 (ori.)	-	10	10	-	100	10	-	10
actuated velocities	0.1	-	0.1	0.1	-	0.1	0.001	-	10	0.1	-	1
unactuated velocities	0.1	-	0.1	1	-	1	1	-	10	0.1	-	1
actuated torque	-	0.1	-	-	0.01	-	-	0.1	-	-	0.001	-
unactuated torque	-	1000	-	-	100	-	-	1000	-	-	1000	-

**Figure 5.** Convergence with quadratic penalty and Lagrange multipliers for each of the four examples.

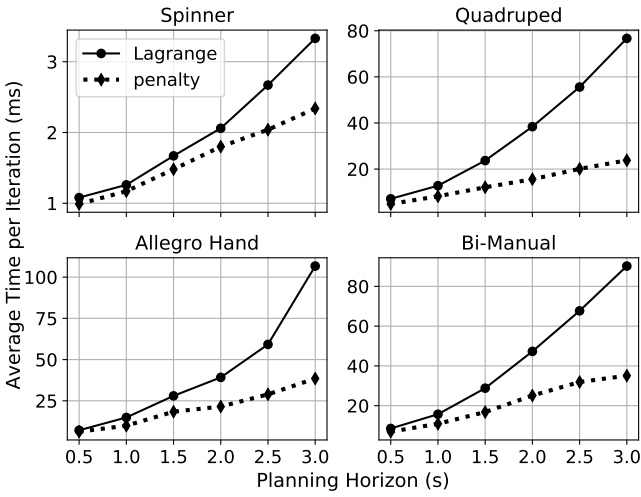
Inverse dynamics derivatives (orange) are the most expensive component. Fortunately, derivatives and cost calculations are easily parallelized.

Table 4 illustrates the sensitivity of our solver to various contact parameterizations. Specifically, it shows the constraint violation magnitude after 500 iterations, a rough measure of performance, on the spinner problem for various contact stiffness ( $k$ ) and stiction velocity ( $v_s$ ) values.

For our default stiction velocity of  $v_s = 0.05$  m/s (top row), the solver performs well at stiffnesses up to  $2 \cdot 10^8$  N/m. This exceeds the stiffness of steel, which has a stiffness on the order of  $10^7$  N/m (Castro et al. 2023). However, as

we decrease the stiction velocity  $v_s$ , the performance of the solver drops off, particularly for large values of  $k$ . Smaller stiction velocities correspond to a closer approximation of coulomb friction. Like high stiffness, low stiction velocity provides a closer approximation of rigid contact at the price of a worse-conditioned trajectory optimization problem. This motivates our choice of contact parameters that are as soft as possible while maintaining good closed-loop performance, as described in Section 4.2.1.





**Figure 6.** Average wall-clock time per iteration for various planning horizons. All examples used a 50 ms time step, with cost and gradient computations parallelized across 4 threads.

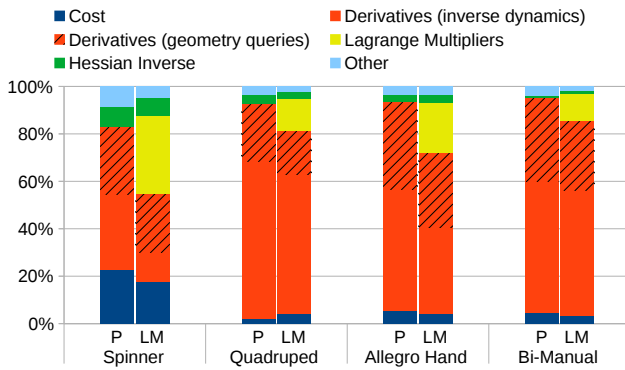


**Figure 7.** Percent of CPU time dedicated to major computational elements, using the penalty method (P) or Lagrange multipliers (LM) to handle equality constraints. Derivative and cost calculations (blue, orange, striped orange) can be trivially parallelized.

**Table 4.** Spinner constraint violation after 500 iterations, under various contact stiffnesses  $k$  and stiction velocities  $v_s$ .

$v_s \backslash k$	$2 \cdot 10^2$	$2 \cdot 10^4$	$2 \cdot 10^6$	$2 \cdot 10^8$
0.05	$6.1 \cdot 10^{-8}$	$2.5 \cdot 10^{-8}$	$7.2 \cdot 10^{-8}$	$2.8 \cdot 10^{-7}$
0.01	$2.8 \cdot 10^{-7}$	$2.3 \cdot 10^{-7}$	$3.0 \cdot 10^{-4}$	$2.8 \cdot 10^{-1}$
0.005	$4.2 \cdot 10^{-5}$	$2.7 \cdot 10^{-3}$	$1.0 \cdot 10^{-3}$	$3.2 \cdot 10^{-1}$
0.001	$1.3 \cdot 10^{-2}$	$7.2 \cdot 10^{-2}$	$1.1 \cdot 10^{-0}$	$5.0 \cdot 10^{-0}$

## 6.4 Model Predictive Control

We applied our solver to CI-MPC for all four example scenarios. We did not run the solver to convergence, but rather performed a single iteration at each MPC step, as in a real-time iteration scheme (Diehl et al. 2005).

Between iterations, we tracked the latest solution with a higher-frequency feed-forward PD controller,

$$\mathbf{u} = \mathbf{u}_{ff} + \mathbf{K}_P(\mathbf{q}_d - \hat{\mathbf{q}}) + \mathbf{K}_D(\mathbf{v}_d - \hat{\mathbf{v}}), \quad (26)$$

where feedforward torques  $\mathbf{u}_{ff}$ , desired positions  $\mathbf{q}_d$ , and desired velocities  $\mathbf{v}_d$  were obtained from a cubic spline interpolation of IDTO solutions, with the latest solution as

the knot points.  $\hat{\mathbf{q}}$  and  $\hat{\mathbf{v}}$  are state estimates, and  $\mathbf{K}_P$  and  $\mathbf{K}_D$  are gain matrices.

**6.4.1 Spinner** The goal is to move the spinner 2 radians past its starting position. For MPC, the starting position was constantly updated to match the current position, such that the spinner kept spinning. Damping in the spinner joint means that the robot must constantly interact with the spinner to accomplish this task.

With the LM method and parallelization across 4 threads on a laptop (Intel i7-6820HQ, 32 GB RAM), MPC ran in real time at about 200 Hz. A “finger gaiting” cycle emerged from the optimization, as shown in the accompanying video. While the optimizer’s contact model allows some force at a distance, simulations with Drake’s contact model do not (Castro et al. 2020).

The spinner is inspired by an example from Posa and Tedrake (2013), which reports around 30 seconds of offline computation to generate similar behavior.

**6.4.2 Mini Cheetah Quadraped** As for the spinner, we updated the quadraped’s goal at each iteration to move the robot forward at about 0.4 m/s. Again, while the planner’s compliant contact model allows force at a distance and includes very large friction regularization, the simulator used Drake’s contact model with tight regularization of friction, physics-based compliance, and no action at a distance.

With the penalty method and parallelization across 4 threads on a laptop, MPC ran in real-time at about 60 Hz. Over flat portions of the terrain, a trot-like gait emerged, with opposite pairs of legs working together. The robot deviated from this gait to cross two small hills. Screenshots from the generated trajectory are shown in Fig. 8, and the full simulation is shown in the supplemental video.

A trotting gait emerged at various speeds over flat ground, as illustrated in Fig. 9. In this figure, we varied only the target velocity, keeping the same contact parameterization and cost function. The gait frequency and time between touch-down and lift-off events were automatically adjusted by IDTO.

**6.4.3 Allegro Dexterous Hand** The robot was to rotate the ball 180 degrees in its hand. Unlike IDTO’s point contact, the simulation used a hydroelastic model of surface patches (Elandt et al. 2019; Masterjohn et al. 2022) to simulate the rich interactions between the hand and the ball.

We found that the LM method was essential to obtaining good performance. With parallelization across 4 threads on a laptop, MPC ran in real-time at 10 Hz. We found that the robot could perform different rotations merely by changing the desired orientation: no further parameter tuning was needed.

The robot completed the 180-degree rotation shown in Fig. 10 in about 15 seconds, without any offline computation. The resulting trajectory is comparable to that obtained by (Pang et al. 2023), which uses a quasi-dynamic model and requires around a minute of offline computing to perform a similar 180-degree in-hand rotation.

**6.4.4 Bi-Manual Manipulator** Finally, we validated our approach on hardware with two Jaco arms. We first designed several behaviors—push a box on the ground, pick up the box, and balance the box on its edge—in simulation. We

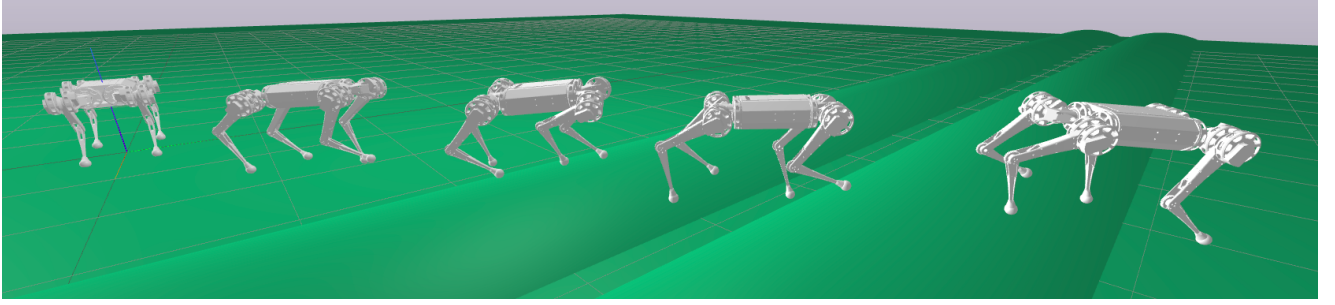


**Figure 8.** A simulated Mini Cheetah quadruped traverses two small hills. The simulation runs in real-time while IDTO acts as an MPC controller at about 60 Hz. We do not specify a preferred contact sequence, only a quadratic cost defining the desired direction of travel. Our CI-MPC planner uses a relaxed model of compliant contact, while the simulator uses Drake’s rigid contact model.

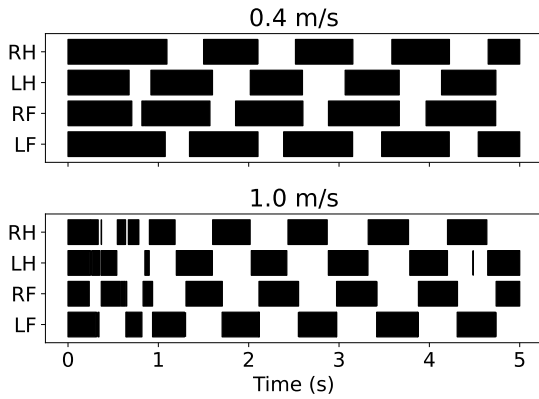


**Figure 9.** Contact pattern for Mini Cheetah moving over flat ground at different target velocities. Black patches indicate a contact phase for the given foot. A trotting gait emerges at various speeds, with IDTO automatically adjusting the gait frequency and amount of overlap between phases.

used hydroelastic contact for the simulation and ran MPC at around 15 Hz on a laptop.

For the hardware experiments, we used a system with a 24-core processor (AMD Ryzen Threadripper 3960x, 64 GB RAM). We parallelized derivative computations across 20 threads (one per time step). Together with the fact that the computer did not need to simultaneously run a simulation, this allowed us to perform MPC between 100-200 Hz. The exact rate varied through the experiments, depending on the contact configuration.

With a few exceptions, we used the same contact parameters in simulation and on hardware. The exceptions primarily had to do with friction since we did not have accurate friction measurements available. We also used a larger friction coefficient (1.0 rather than 0.2) for the planner in the lifting task, as this encouraged the robot to squeeze the box more gently, and we wanted to push the box out of the robot’s grasp, as shown in Fig. 11.

The hardware setup differed slightly from that of the simulation. We operated the robot in position-control mode using Jaco’s proprietary controller with default gains. For the box, an *Optitrack* motion capture system measured pose, and we assumed zero velocity.

Footage of the hardware experiments can be found in the accompanying video. Screenshots of the picking-up task are shown in Fig. 11. These experiments highlight

the usefulness of CI-MPC: our solver was able to recover from significant external disturbances, making and breaking contact, changing between sticking and sliding modes and adjusting contact configurations on the fly.

Our experiments also illustrate some limitations of IDTO, particularly with respect to local minima. This is especially evident in the pushing example, where the robot is tasked with pushing the box on the table to a desired pose. The robot responds quickly and effectively to small disturbances but is not able to recover from a large disturbance that takes the box far from the arms. With the box far away, there are no gradients that indicate to the solver that the arms should reach around the box to push it back: the system is stuck in a local minimum where the arms do not move.

The severity of such local minima can be reduced by increasing the smoothing parameter  $\sigma$ , but there is a tradeoff: with a very large  $\sigma$  the planner expects a considerable amount of force at a distance and may fail to actually make contact. A more problem-specific solution would be to add a cost terms that encourage the end-effector to move to the side of the manipuland opposite the target pose (Aydinoglu et al. 2023).

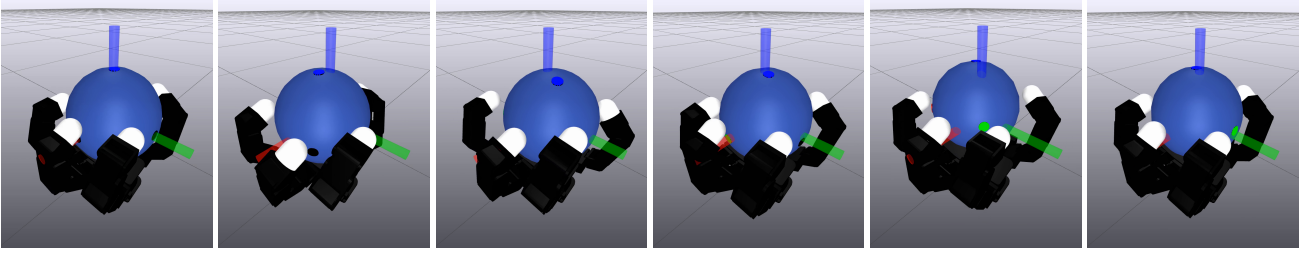
## 6.5 Constraints and Performance

Our solver often takes many iterations to satisfy constraints to tight tolerances (Fig. 5), a likely consequence of our Gauss-Newton Hessian approximation (Nocedal and Wright 2006). How do constraint violations impact CI-MPC performance? Is it important that a CI-MPC solver satisfy constraints to numerical precision?

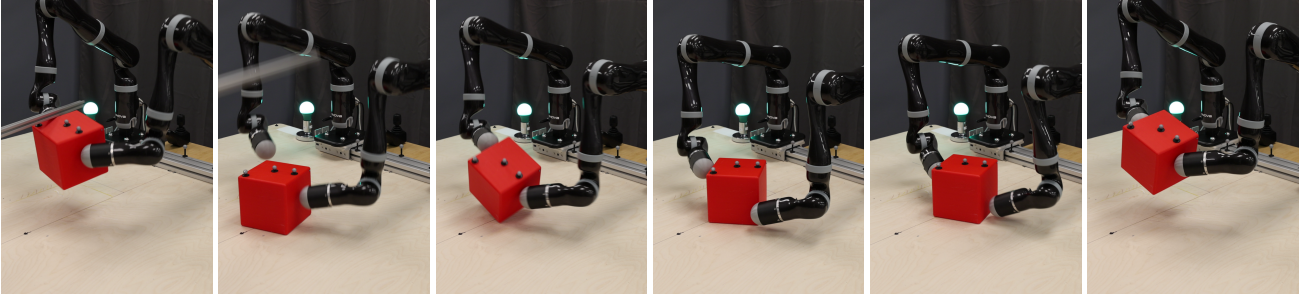
In this section, we show that tight constraint satisfaction is not critical to closed-loop CI-MPC performance. We focus in particular on the spinner as a simple illustrative example.

Figure 12 plots constraint violation over time during CI-MPC, where a single IDTO iteration is performed at each CI-MPC step. We compare two cases. In the first, a fixed target configuration  $\bar{q}$  is used, and constraint violations are eventually driven to zero (dashed lines). In the second, we constantly shift the target configuration so that the spinner is always rotating. In this case, constraint violations do not go to zero. Spikes in constraint violation correspond to contact events, as the finger repeatedly flicks the spinner.

Many practical CI-MPC applications are more similar to the second case. Even if the objective does not shift over time, a changing environment leads to an optimization landscape that is constantly shifting. This is consistent with



**Figure 10.** A simulated Allegro dexterous hand rotates a sphere 180 degrees. IDTO determines when and where to make and break contact at about 10 Hz. The planner uses the simple point contact model described in Section 4.2, while the simulator uses a more realistic hydroelastic model based on contact patches (Elandt et al. 2019; Masterjohn et al. 2022).



**Figure 11.** Two 7-DoF Kinova Jaco arms tasked with lifting a box recover from an external disturbance (push with a stick from above). After dropping the box, the robot attempts to re-grasp but fails. The robot then selects a new contact configuration and succeeds on the second attempt.

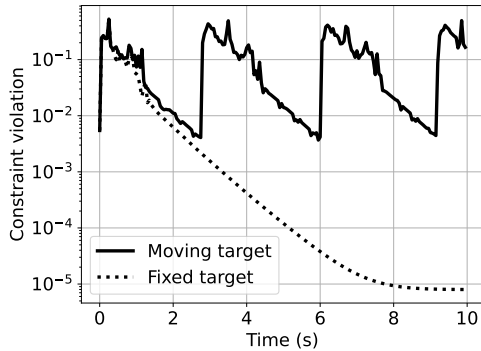


**Figure 12.** Constraint violations during closed-loop MPC with the spinner. When the target configuration  $\bar{q}$  is fixed, we see convergence over time (dotted line). If we continually update the target configuration so the spinner is constantly rotating (solid line), constraint violations don’t grow unbounded, but don’t converge either. Both examples correspond to good qualitative performance.

the analogy of “surfing” rather than “mountain climbing” for CI-MPC (Howell et al. 2022a): tight constraint satisfaction and optimality is less important than fast iteration times and sufficient improvement at each iteration.

Figure 13 plots the spinner angle predicted by IDTO with an actual simulated rollout at different constraint violation levels. Unsurprisingly, lower constraint violations correspond to a closer match between the predicted and actual trajectories. However, even when constraint violations are quite large (top subplot), the predicted trajectory roughly captures the key aspects of the system’s behavior: in this case, the fact that the spinner rotates once the finger pushes it.

Similarly, IDTO’s predictions are not perfect even at convergence (bottom subfigure). This is due to a mismatch between the contact models and integration schemes of the simulator and the planner. Persistent prediction error even at convergence further emphasizes the fact that tight constraint satisfaction is not critical, a result consistent with recent results in the literature (Khazoom et al. 2024).

Because tight constraint satisfaction is less critical than fast iteration times, we generally prefer the simple quadratic penalty method (Section 5.2.1) to the Lagrange multipliers method (Section 5.2.2) for handling constraints. While there are some cases where Lagrange multipliers can reduce the severity of local minima, the cost of slower iteration times is rarely worth it. As a result, we recommend that users start with the penalty method, and only switch to the Lagrange multipliers method if constraint violations pose a challenge or if it reduces local minima on a particular problem.

## 7 Comparison with Existing Work

Table 5 compares IDTO to results reported in the literature. For brevity, we focus on recent results that run CI-MPC in real time. Because CI-MPC performance often depends heavily on implementation details and parameter tuning, we choose to compare with results reported in the literature rather than attempting to reimplement the methods ourselves. We believe this facilitates the fairest possible comparison, as authors are incentivised to report their best results.

We encourage the reader to read the cited references for further details. Notice that the oldest work is from 2018, with most from 2022 or newer, so major performance differences cannot be attributed to differences in processing power. Nonetheless, hardware and software quality do significantly impact performance, and most methods in Table 5 would



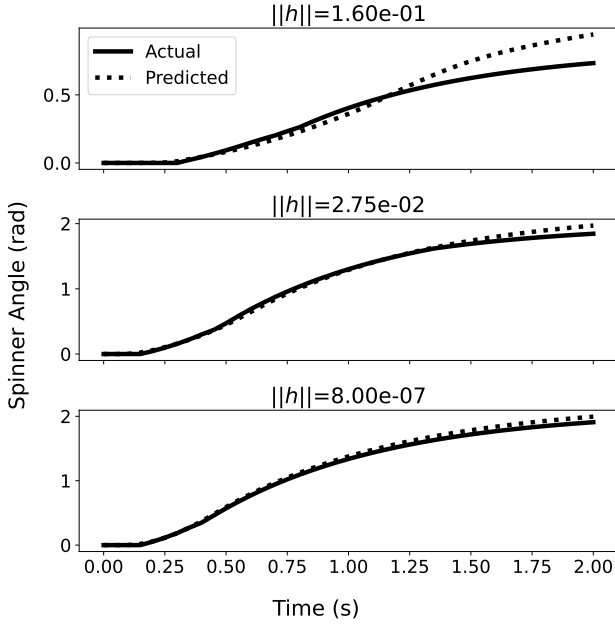


**Figure 13.** Comparison between the spinner angle predicted by MPC (dotted lines) and the actual trajectory when MPC's controls are applied open-loop (solid lines), across various constraint violation levels. IDTO's predictions capture the key features of the system's behavior, even when constraint violations are large (top).

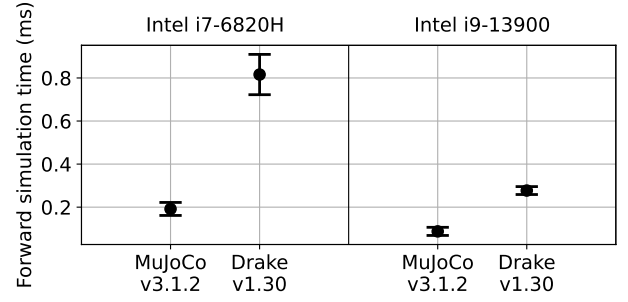
perform better with further optimization. This includes our own approach: while Drake is currently undergoing significant performance improvements, IDTO would benefit from faster multibody algebra. For example, MuJoCo can simulate a humanoid with 4000 timesteps per second on a single CPU (Howell et al. 2022a). By contrast, Drake runs a comparably sized model at around 800 timesteps per second.

Table 5 shows that IDTO allows longer planning horizons than many existing methods, a fact that is enabled by relatively large time steps. We do not simplify the system dynamics, though we do simplify collision geometries (see Remark 3). We are particularly proud of the fact that IDTO does not require a preferred contact sequence for the quadruped, though specifying one is possible in the IDTO framework and might improve performance in practice.

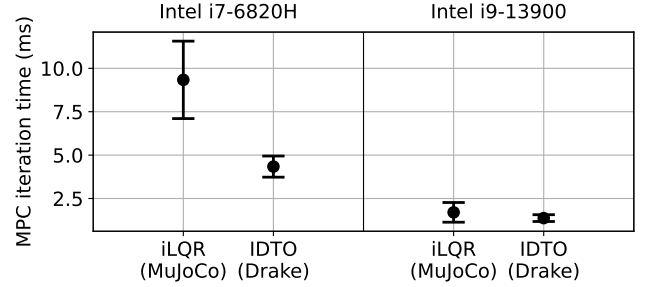
### 7.1 Benefits of Inverse Dynamics

In this section, we compare the performance of IDTO and a state-of-the-art forward-dynamics-based CI-MPC method: the contact-implicit iLQR implementation of MuJoCo MPC (Howell et al. 2022a). While an accurate head-to-head comparison is difficult due to the complexity of CI-MPC methods and the importance of implementation details, we believe the fact that MuJoCo MPC also offers a performant and well-maintained C++ implementation makes for as fair a comparison as possible.

We focus on the spinner example, for which both methods obtain good closed-loop performance. While this example is relatively simple, it captures two key benefits of IDTO over a forward dynamics formulation: faster iteration times and reduced susceptibility to local minima.



**(a)** Time to simulate the spinner for 2.0 seconds with random control actions. MuJoCo is consistently faster than Drake.



**(b)** MPC iteration times for the spinner with a 2.0 second planning horizon. IDTO is generally faster than forward-dynamics-based iLQR.

**Figure 14.** Iteration times for our IDTO implementation are on par with or faster than the forward-dynamics-based iLQR of Howell et al. (2022a) (b), despite using a slower dynamics backend (a). The trends are consistent across an older laptop (i7 CPU) and a newer desktop (i9 CPU).

**7.1.1 Faster Iteration Times** First, note that the MuJoCo dynamics backend used by the iLQR baseline is consistently faster than the Drake dynamics backend used by our IDTO solver. This is shown in Fig. 14a, where we compare the time to simulate the spinner open loop for 2.0 seconds with random control actions. We use a time step of 0.05 seconds for both methods, and average over 10,000 trials. Mean and standard deviation are shown for both an older laptop (i7 CPU) and a newer desktop (i9 CPU). This provides a significant baseline advantage to iLQR, as it is implemented over a faster dynamics backend.

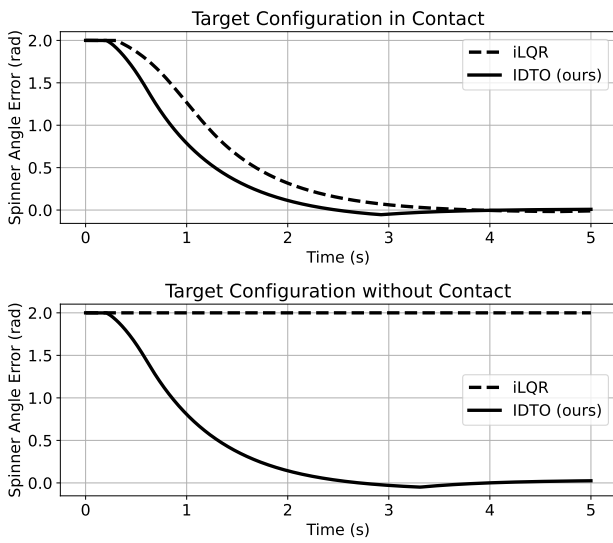
Nonetheless, IDTO generally achieves faster iteration times than iLQR, as shown in Fig. 14b. We use the same cost function and planning horizon (2.0 seconds with a 0.05 s time step) for both methods, and average over 10,000 iterations. IDTO is faster because iLQR requires a full forward simulation at each iteration, resolving contact dynamics and other details to high precision with an optimization sub-problem at each time step. In contrast, IDTO only requires simpler inverse dynamics computations, and does not involve an inner optimization problem.

**7.1.2 Fewer Local Minima** Another advantage of IDTO is reduced sensitivity to local minima. To illustrate this, we compare the closed-loop performance of IDTO and iLQR on two variations of the spinner problem (Fig. 15). In the first case (top subplot), the target configuration  $\bar{q}$  puts the finger in contact with the spinner. Both IDTO and iLQR successfully rotate the spinner to the desired angle in this case. On the second (bottom subplot), the target configuration  $\bar{q}$  puts the



**Table 5.** Comparison with real-time CI-MPC in the literature. Data marked with ? was not reported.

Method	System	DoFs	Horizon (s)	$\delta t$ (s)	MPC Iters.	Freq.	Simplified Dynamics	Pref. Contact Sequence	Hardware
Neunert et al. (2018)	Quadruped	18	0.5	0.004	1	190 Hz	No	Yes	Yes
Kong et al. (2022)	Quadruped	18	0.5	0.01	1	?	No	Yes	Yes
Howell et al. (2022a)	Quadruped	18	0.25	0.01	1	100 Hz	No	Yes	No
Howell et al. (2022a)	Shadow Hand	26	0.25	0.01	1	100 Hz	No	No	No
Cleac'h et al. (2023)	Push Bot	2	1.6	0.04	?	70 Hz	No	No	No
Cleac'h et al. (2023)	Quadruped	18	0.15	0.05	?	100 Hz	Yes	Yes	Yes
Aydinoglu et al. (2023)	Finger Pivot	5	0.1	0.01	5	45 Hz	No	No	No
Aydinoglu et al. (2023)	Ball Roll	9	0.5	0.1	2	80 Hz	Yes	No	Yes
Kim et al. (2023)	Quadruped	18	0.5	0.025	4	40 Hz	No	Yes	Yes
IDTO (ours)	Spinner	3	2.0	0.05	1	200 Hz	No	No	No
IDTO (ours)	Hopper	5	2.0	0.05	1	100 Hz	No	No	No
IDTO (ours)	Quadruped	18	1.0	0.05	1	60 Hz	No	No	No
IDTO (ours)	Bi-Manual	20	1.0	0.05	1	100 Hz	No	No	Yes
IDTO (ours)	Allegro Hand	22	2.0	0.05	1	10 Hz	No	No	No

**Figure 15.** IDTO reduces the severity of local minima compared to (forward-dynamics-based) iLQR. Both methods are able to drive the spinner to the desired angle when the target configuration  $\bar{q}$  involves contact between the finger and the side of the spinner (top). However, when the target configuration places the finger out of contact, iLQR gets stuck in a local minimum where the spinner does not move (bottom).

finger a short distance away from the spinner. In this case, IDTO successfully rotates the spinner, while iLQR is stuck in a local minimum where the spinner does not move.

While some of this reduction in local minima severity can be attributed to our contact model’s allowance for some force at a distance, there are also more fundamental reasons that IDTO reduces local minima, even without force at a distance. As an example of this, consider a simple case of a block resting on a rigid platform, as shown in Fig. 16.

The block is actuated by a force acting on its center of mass, and the task is to move upward. With a forward dynamics formulation, the system is stuck in a local minimum, as applying a small force has no effect on the block’s position [Le Lidec et al. \(2024\)](#). In contrast, under an inverse dynamics formulation, there are clearly defined gradients with respect to the configuration  $q$ , eliminating the local minimum.

**Figure 16.** A block rests on a rigid platform. The task is to apply control forces  $u$  to lift the block. For forward-dynamics-based CI-MPC this is a local minimum, since small control inputs  $u$  do not change the block’s position ([Le Lidec et al. 2024](#)). An inverse dynamics formulation, where the decision variables are  $q$ , does not contain this local minimum: there is a clear gradient showing that the optimal behavior is to lift the box.

## 8 Limitations

In this section, we highlight the weaknesses of our approach, with an eye toward future CI-MPC research.

First, IDTO only guarantees dynamic feasibility at convergence due to the constraint (13b). In practice, non-converged solutions include forces on unactuated DoFs. For example, the spinner might spin without anything pushing it. With the quadratic penalty method these non-physical forces can exist even at convergence. The LM method helps, but does not eliminate the problem completely. In particular, LM is more costly than the penalty method and reduces the impact of parallelization (Fig. 7). Furthermore, equality constraints are still only enforced at convergence. LM performance could likely be improved with sparse algebra in the computation of (17).

Solver convergence can be slow, as shown in Fig. 5. This is an inevitable result of the Gauss-Newton approximation — problem (13) is a large-residual problem, for which Gauss-Newton methods converge linearly ([Nocedal and Wright 2006](#)). Accelerating convergence with second-order techniques is a potentially fruitful area for future research.

Our solver does not currently support arbitrary constraints, such as input torque or joint angle limits. While approximating such constraints with a penalty method would be straightforward, this may not be suitable for athletic behaviors at the limit of a robot’s capabilities.

Computationally, the biggest bottleneck is computing derivatives. This is shown in orange and striped orange in Fig. 7. Recent advances in analytical derivatives of rigid-body dynamics algorithms ([Singh et al. 2022](#); [Carpentier](#)

et al. 2019) could potentially alleviate this bottleneck, but such results would first need to be extended to include differentiation through contact, and in particular to account for the dependence of the jacobian on contact location.

Practically, our solver’s reliance on spherical collision geometries, as discussed in Remark 3, presents a major limitation. While inscribed spheres enabled basic box manipulation on hardware, this approximation introduces modeling errors that could be problematic for more complex tasks. A better long-term solution could be a model like hydroelastics (Elandt et al. 2019; Masterjohn et al. 2022) that avoids discontinuous artifacts for objects with sharp edges, or a method that leverages the KKT conditions of the optimization problem for the signed distance function to obtain a smooth approximation (Dietz et al. 2024).

As for most CITO solvers, cost weights and contact parameters determine IDTO’s performance in practice. While we found that IDTO was not particularly sensitive to changes in the cost weights, as evidenced by the multiples of 10 in Table 3, IDTO is sensitive to contact modeling parameters, particularly the stiction velocity (Table 4). Nonetheless, we found that a fast solver made contact parameter tuning easier. This could be further improved with a graphical interface (Howell et al. 2022a).

Finally, IDTO is a fundamentally local optimization method and as such is vulnerable to local minima. A more systematic “virtual force” framework (Önol et al. 2020; Todorov 2019b) could help reduce the severity of these local minima. Integration with a higher-level global planner is another promising avenue toward better performance. The fact that local optimization with IDTO is sufficient for tasks as complex as generating quadruped gaits and in-hand object rotation with a dexterous hand presents an opportunity to reduce the burden on a higher-level global planner, which might merely give some suggestion of promising contact areas rather than specifying a complete contact sequence.

## 9 Conclusion

IDTO is a simple but surprisingly effective tool for planning and control through contact. Even with a relaxed contact model and simple quadratic costs, IDTO enables real-time CI-MPC in simulation (with rigid contact) and on hardware, and is competitive with the state of the art. We believe that the simplicity of IDTO is responsible for much of its performance, and hope that it can provide a foundation for further improvements in the future.

Areas for future research include improving contact discovery with virtual forces, developing faster (analytical) derivatives for inverse dynamics with contact, considering convex contact models (Castro et al. 2022), and extracting a local feedback policy in the style of iLQR/DDP. While we chose an implicit integration scheme out of a desire for numerical stability, higher-accuracy semi-implicit integration schemes are compatible with the IDTO framework, and could improve performance. Further improvements could stem from proper handling of  $SE(3)$  structure in the dynamics and second-order methods for faster convergence.

Finally, to mitigate the local nature of IDTO, our solver could be combined with a higher-level global planner based

on sampling (Pang et al. 2023), graph search (Natarajan et al. 2023), learning (Chi et al. 2023), or combinatorial motion planning (Marcucci et al. 2021).

## Acknowledgements

Thanks to Sam Creasey for helping with the Jaco hardware, Jarod Wilson for 3D printing parts, Andrew Patrikalakis for setting up an external repository, and the Tactile/Punyo and Dynamics/Simulation teams at Toyota Research Institute for their resources and support.

## Appendix

### Computing the Hessian Approximation

As outlined in Section 5.3, we compute a Gauss-Newton approximation of the Hessian. This approximation neglects second-order time derivatives of the inverse dynamics when propagating derivatives through (23).

Separating the weight matrix  $Q = \text{diag}([Q_q \ Q_v])$  into position and velocity components and noting the symmetry of  $H$ , we compute nonzero blocks as follows:

$$H_{k,k-2} = \left[ \frac{\partial \tau_{k-1}}{\partial q_{k-2}} \right]^T R \frac{\partial \tau_{k-1}}{\partial q_k},$$

$$H_{k,k-1} = \left[ \frac{\partial v_t}{\partial q_{k-1}} \right]^T Q_v \frac{\partial v_t}{\partial q_k} + \left[ \frac{\partial \tau_{k-1}}{\partial q_{k-1}} \right]^T R \frac{\partial \tau_{k-1}}{\partial q_k} + \left[ \frac{\partial \tau_k}{\partial q_{k-1}} \right]^T R \frac{\partial \tau_k}{\partial q_k},$$

$$H_{k,k} = Q_q + \left[ \frac{\partial v_t}{\partial q_t} \right]^T Q_v \frac{\partial v_t}{\partial q_t} + \left[ \frac{\partial v_{k+1}}{\partial q_t} \right]^T Q_v \frac{\partial v_{k+1}}{\partial q_t} + \left[ \frac{\partial \tau_{k-1}}{\partial q_t} \right]^T R \frac{\partial \tau_{k-1}}{\partial q_k} + \left[ \frac{\partial \tau_k}{\partial q_t} \right]^T R \frac{\partial \tau_k}{\partial q_k} + \left[ \frac{\partial \tau_{k+1}}{\partial q_t} \right]^T R \frac{\partial \tau_{k+1}}{\partial q_k}.$$

Constructing this Hessian approximation requires only velocity and inverse dynamics derivatives —  $\frac{\partial v_k}{\partial q_k}$ ,  $\frac{\partial v_{k+1}}{\partial q_k}$ ,  $\frac{\partial \tau_{k-1}}{\partial q_k}$ ,  $\frac{\partial \tau_k}{\partial q_k}$ , and  $\frac{\partial \tau_{k+1}}{\partial q_k}$  — as discussed in Section 5.3. Our solver calculates these derivatives once per iteration and caches them for computational efficiency.

## References

- Aydinoglu A, Wei A and Posa M (2023) Consensus complementarity control for multi-contact mpc. *arXiv preprint arXiv:2304.11259*.
- Benkert K and Fischer R (2007) An efficient implementation of the thomas-algorithm for block penta-diagonal systems on vector computers. In: *International Conference on Computational Science*. Springer, pp. 144–151.
- Carius J, Ranftl R, Koltun V and Hutter M (2018) Trajectory optimization with implicit hard contacts. *IEEE Robotics and Automation Letters* 3(4): 3316–3323.
- Carpentier J and Mansard N (2018) Analytical derivatives of rigid body dynamics algorithms. In: *Robotics: Science and systems (RSS 2018)*.
- Carpentier J, Saurel G, Buondonno G, Mirabel J, Lamiraux F, Stasse O and Mansard N (2019) The pinocchio c++ library: A fast and flexible implementation of rigid body dynamics algorithms and their analytical derivatives. In: *2019 IEEE/SICE*

- International Symposium on System Integration (SII)*. IEEE, pp. 614–619.
- Castro A, Han X and Masterjohn J (2023) Irrotational contact fields. *arXiv preprint arXiv:2312.03908*.
- Castro AM, Permenter FN and Han X (2022) An unconstrained convex formulation of compliant contact. *IEEE Transactions on Robotics* 39(2): 1301–1320.
- Castro AM, Qu A, Kuppuswamy N, Alspach A and Sherman M (2020) A transition-aware method for the simulation of compliant contact with regularized friction. *IEEE Robotics and Automation Letters* 5(2): 1859–1866.
- Chatzinikolaïdis I and Li Z (2021) Trajectory optimization of contact-rich motions using implicit differential dynamic programming. *IEEE Robotics and Automation Letters* 6(2): 2626–2633.
- Chi C, Feng S, Du Y, Xu Z, Cousineau E, Burchfiel B and Song S (2023) Diffusion policy: Visuomotor policy learning via action diffusion. *arXiv preprint arXiv:2303.04137*.
- Cleac’h SL, Howell T, Schwager M and Manchester Z (2023) Fast contact-implicit model-predictive control. *arXiv preprint arXiv:2107.05616*.
- Cui L and Dai J (2010) Geometric kinematics of rigid bodies with point contact. In: *Advances in Robot Kinematics: Motion in Man and Machine: Motion in Man and Machine*. Springer, pp. 429–436.
- Diehl M, Bock HG and Schlöder JP (2005) A real-time iteration scheme for nonlinear optimization in optimal feedback control. *SIAM Journal on control and optimization* 43(5): 1714–1736.
- Dietz C, Nurkanović A, Albrecht S and Diehl M (2024) High accuracy numerical optimal control for rigid bodies with patch contacts through equivalent contact points—extended version. *arXiv preprint arXiv:2403.13931*.
- Elandt R, Drumwright E, Sherman M and Ruina A (2019) A pressure field model for fast, robust approximation of net contact force and moment between nominally rigid objects. In: *2019 IEEE/RSJ International Conference on Intelligent Robots and Systems (IROS)*. IEEE, pp. 8238–8245.
- Erez T and Todorov E (2012) Trajectory optimization for domains with contacts using inverse dynamics. In: *2012 IEEE/RSJ International Conference on Intelligent Robots and Systems*. IEEE, pp. 4914–4919.
- Ferrolho H, Ivan V, Merkt W, Havoutis I and Vijayakumar S (2021) Inverse dynamics vs. forward dynamics in direct transcription formulations for trajectory optimization. In: *2021 IEEE International Conference on Robotics and Automation (ICRA)*. IEEE, pp. 12752–12758.
- Gifftthaler M, Neunert M, Stäuble M, Buchli J and Diehl M (2018) A family of iterative gauss-newton shooting methods for nonlinear optimal control. In: *2018 IEEE/RSJ International Conference on Intelligent Robots and Systems (IROS)*. IEEE, pp. 1–9.
- Gilbert EG, Johnson DW and Keerthi SS (1988) A fast procedure for computing the distance between complex objects in three-dimensional space. *IEEE Journal on Robotics and Automation* 4(2): 193–203.
- Howell T, Gileadi N, Tunyasuvunakool S, Zakka K, Erez T and Tassa Y (2022a) Predictive sampling: Real-time behaviour synthesis with mujoco. *arXiv preprint arXiv:2212.00541*.
- Howell TA, Le Cleac’h S, Kolter JZ, Schwager M and Manchester Z (2022b) Dojo: A differentiable simulator for robotics. *arXiv preprint arXiv:2203.00806* 9.
- Howell TA, Le Cleac’h S, Singh S, Florence P, Manchester Z and Sindhvani V (2022c) Trajectory optimization with optimization-based dynamics. *IEEE Robotics and Automation Letters* 7(3): 6750–6757.
- Hunt K and Crossley F (1975) Coefficient of restitution interpreted as damping in vibroimpact. *Journal of Applied Mechanics* 42(2): 440–445.
- Katz B, Di Carlo J and Kim S (2019) Mini cheetah: A platform for pushing the limits of dynamic quadruped control. In: *2019 international conference on robotics and automation (ICRA)*. IEEE, pp. 6295–6301.
- Khazoom C, Hong S, Chignoli M, Stanger-Jones E and Kim S (2024) Tailoring solution accuracy for fast whole-body model predictive control of legged robots. *IEEE Robotics and Automation Letters*.
- Kim G, Kang D, Kim JH, Hong S and Park HW (2023) Contact-implicit mpc: Controlling diverse quadruped motions without pre-planned contact modes or trajectories. *arXiv preprint arXiv:2312.08961*.
- Kim G, Kang D, Kim JH and Park HW (2022) Contact-implicit differential dynamic programming for model predictive control with relaxed complementarity constraints. In: *2022 IEEE/RSJ International Conference on Intelligent Robots and Systems (IROS)*. IEEE, pp. 11978–11985.
- Kong NJ, Li C and Johnson AM (2022) Hybrid iLQR model predictive control for contact implicit stabilization on legged robots. *arXiv preprint arXiv:2207.04591*.
- Le Lidec Q, Schramm F, Montaut L, Schmid C, Laptev I and Carpentier J (2024) Leveraging randomized smoothing for optimal control of nonsmooth dynamical systems. *Nonlinear Analysis: Hybrid Systems* 52: 101468.
- Li W and Todorov E (2004) Iterative linear quadratic regulator design for nonlinear biological movement systems. In: *ICINCO (1)*. Citeseer, pp. 222–229.
- Manchester Z, Doshi N, Wood RJ and Kuindersma S (2019) Contact-implicit trajectory optimization using variational integrators. *The International Journal of Robotics Research* 38(12-13): 1463–1476.
- Marcucci T, Umenberger J, Parrilo PA and Tedrake R (2021) Shortest paths in graphs of convex sets. *arXiv preprint arXiv:2101.11565*.
- Masterjohn J, Guoy D, Shepherd J and Castro A (2022) Velocity level approximation of pressure field contact patches. *IEEE Robotics and Automation Letters* 7(4): 11593–11600.
- Mayne D (1966) A second-order gradient method for determining optimal trajectories of non-linear discrete-time systems. *International Journal of Control* 3(1): 85–95.
- Mordatch I, Popović Z and Todorov E (2012a) Contact-invariant optimization for hand manipulation. In: *Proceedings of the ACM SIGGRAPH/Eurographics symposium on computer animation*. pp. 137–144.
- Mordatch I, Todorov E and Popović Z (2012b) Discovery of complex behaviors through contact-invariant optimization. *ACM Transactions on Graphics (TOG)* 31(4): 1–8.
- Moré JJ (2006) The levenberg-marquardt algorithm: implementation and theory. In: *Numerical analysis: proceedings of the biennial Conference held at Dundee, June 28–July 1, 1977*. Springer, pp. 105–116.

- Moura J, Stouraitis T and Vijayakumar S (2022) Non-prehensile planar manipulation via trajectory optimization with complementarity constraints. In: *2022 International Conference on Robotics and Automation (ICRA)*. IEEE, pp. 970–976.
- Natarajan R, Johnston GL, Simaan N, Likhachev M and Choset H (2023) Torque-limited manipulation planning through contact by interleaving graph search and trajectory optimization. In: *2023 IEEE International Conference on Robotics and Automation (ICRA)*.
- Neunert M, Farshidian F, Winkler AW and Buchli J (2017) Trajectory optimization through contacts and automatic gait discovery for quadrupeds. *IEEE Robotics and Automation Letters* 2(3): 1502–1509.
- Neunert M, Stäubli M, Gifftthaler M, Bellicoso CD, Carius J, Gehring C, Hutter M and Buchli J (2018) Whole-body nonlinear model predictive control through contacts for quadrupeds. *IEEE Robotics and Automation Letters* 3(3): 1458–1465.
- Nocedal J and Wright SJ (2006) *Numerical optimization*. Second edition. New York: Springer.
- Önol AÖ, Corcodel R, Long P and Padır T (2020) Tuning-free contact-implicit trajectory optimization. In: *2020 IEEE International Conference on Robotics and Automation (ICRA)*. IEEE, pp. 1183–1189.
- Önol AÖ, Long P and Padır T (2019) Contact-implicit trajectory optimization based on a variable smooth contact model and successive convexification. In: *2019 International Conference on Robotics and Automation (ICRA)*. IEEE, pp. 2447–2453.
- Pang T, Suh HT, Yang L and Tedrake R (2023) Global planning for contact-rich manipulation via local smoothing of quasi-dynamic contact models. *IEEE Transactions on Robotics*.
- Patel A, Shield SL, Kazi S, Johnson AM and Biegler LT (2019) Contact-implicit trajectory optimization using orthogonal collocation. *IEEE Robotics and Automation Letters* 4(2): 2242–2249.
- Posa M, Kuindersma S and Tedrake R (2016) Optimization and stabilization of trajectories for constrained dynamical systems. In: *2016 IEEE International Conference on Robotics and Automation (ICRA)*. IEEE, pp. 1366–1373.
- Posa M and Tedrake R (2013) Direct trajectory optimization of rigid body dynamical systems through contact. In: *Algorithmic foundations of robotics*. Springer, pp. 527–542.
- Singh S, Russell RP and Wensing PM (2022) Efficient analytical derivatives of rigid-body dynamics using spatial vector algebra. *IEEE Robotics and Automation Letters* 7(2): 1776–1783.
- Suh HJT, Pang T and Tedrake R (2022) Bundled gradients through contact via randomized smoothing. *IEEE Robotics and Automation Letters* 7(2): 4000–4007.
- Tassa Y, Erez T and Todorov E (2012) Synthesis and stabilization of complex behaviors through online trajectory optimization. In: *2012 IEEE/RSJ International Conference on Intelligent Robots and Systems*. IEEE, pp. 4906–4913.
- Tedrake R and the Drake Development Team (2019) Drake: Model-based design and verification for robotics. URL <https://drake.mit.edu>.
- Todorov E (2019a) Acceleration based methods. <https://youtu.be/uWADBSmHebA>.
- Todorov E (2019b) Optico: A framework for model-based optimization with mujoco physics. Invited Talk, Neural Information Processing Systems. <https://slideslive.com/38922729/>.
- Wang M, Önol AÖ, Long P and Padır T (2023) Contact-implicit planning and control for non-prehensile manipulation using state-triggered constraints. In: *Robotics Research*. Springer, pp. 189–204.
- Wensing PM, Posa M, Hu Y, Escande A, Mansard N and Del Prete A (2022) Optimization-based control for dynamic legged robots. *arXiv preprint arXiv:2211.11644*.
- Winkler AW, Bellicoso CD, Hutter M and Buchli J (2018) Gait and trajectory optimization for legged systems through phase-based end-effector parameterization. *IEEE Robotics and Automation Letters* 3(3): 1560–1567.